Correlation between electrical properties and thermodynamic stability of $ACoO_{3-\delta}$ perovskites (A = La, Pr, Nd, Sm, Gd)

Barbara Scherrer,[1,*] Ashley S. Harvey,[1] Speranta Tanasescu,[2] Florina Teodorescu,[2] Alina Botea,[2] Kazimierz Conder,[3] A. Nicholas Grundy,[1,4] Julia Martynczuk,[1] and Ludwig J. Gauckler[1]

[1]*Department of Materials, ETH Zurich, Wolfgang-Pauli-Str. 10, 8093 Zurich, Switzerland*

[2]*Institute of Physical Chemistry "Ilie Murgulescu," Splaiul Independentei 202, 060021 Bucharest, Romania*

[3]*Laboratory for Developments and Methods, Paul Scherrer Institut, 5232 Villigen-PSI, Switzerland*

[4]*CONCAST AG, Toedistrasse 9, 8027 Zurich, Switzerland*

(Received 8 February 2011; revised manuscript received 27 April 2011; published 22 August 2011)

For perovskites with the general formula $ACoO_{3-\delta}$ (A = La, Pr, Nd, Sm, and Gd) the influence of the A-site cation on the electrical conductivity, electronic structure, thermodynamic stability, and oxygen stoichiometry was studied. The perovskite oxide powders were produced by a combined citric acid and ethylenediaminetetraacetic acid complexing method. Ceramic specimens sintered at 1100 °C in air were single-phase perovskites. With increasing temperature, the electrical conductivity shows three discrete regimes. All compositions show semiconductivity up to a transition temperature of ~300 °C–450 °C and then behave like metallic conductors. The activation energies for the semiconductivity, as well as the transition temperatures to the metallic-like conduction, decrease monotonically with increasing pseudocubic lattice parameters, i.e., with increasing ionic radii of the A cation. This behavior correlates with decreasing oxygen nonstoichiometry and increased thermodynamic stability. The highest conductivity and the lowest activation energy of 0.66 eV were found for $LaCoO_{3-\delta}$, which also had the lowest semiconductor–metal transition temperature at 269 °C, the lowest oxygen nonstoichiometry of $\delta = 0.008$, and the highest Gibbs free energy change for the decomposition reaction of 42.37 kJ/mol at 850 °C. $GdCoO_{3-\delta}$ had the highest oxygen nonstoichiometry with $\delta = 0.032$, a high activation energy of 1.19 eV for the semiconductivity with a high transition temperature at 452 °C, and the lowest Gibbs free energy change of 26.54 kJ/mol at 850 °C. X-ray absorption spectroscopy data imply an increasing Co low-spin character with decreasing cation radius from La to Gd, while an increase in temperature increases the number of holes or Co 3d bandwidth. This correlates well with the electrical conductivity data.

DOI: 10.1103/PhysRevB.84.085113 PACS number(s): 72.60.+g, 81.05.Je, 61.72.jd, 71.30.+h

I. INTRODUCTION

Perovskite oxides are important electroceramics and catalysts for electrodes in solid oxide fuel cells (SOFCs),[1] chemical sensors,[2] oxygen separation membranes, heterogeneous catalysts,[3] reading heads in computer hard disks showing giant magnetoresistivity,[4] and high-temperature superconductors.[5] In addition, large parts of Earth's mantle crust consist of the perovskite $CaSiO_3$, making this a diverse family of materials.[6–8]

Perovskites form a prominent family of phases among the mixed metal oxides with the general formula ABO_3. The possibility to synthesize multicomponent perovskites with the general formula $A_{1-x}A'_xB_{1-y}B'_yO_3$ greatly increases opportunities for tuning their electrical and thermodynamic properties. A denotes the rare earth element, and B denotes the transition metal. The occurrence of the perovskite structure was characterized by Goldschmidt,[9] who introduced a tolerance factor t correlating the radii r_A and r_B of the A and B cations, with r_O as the oxygen anion radius:

$$t = \frac{r_A + r_O}{\sqrt{2}(r_B + r_O)} \quad (1)$$

The tolerance factor equation describes the fit of the A-site cation in the corner sharing BO_6 octahedra. The ideal cubic perovskite structure is found to be stable at room temperature in cases where the t value is very close to 1. Generally, perovskites occur for $0.75 \leqslant t \leqslant 1.0$, including the distorted perovskites. The distortion not only affects the crystal structure but also has a profound influence on a number of physical properties, such as electrical conductivity, magnetic superexchange interactions, and certain dielectric properties. Another method based on the crystal structure to compare perovskites with different symmetry is to calculate, from the cell volume, the pseudocubic lattice constant per formula, which gives an idea of the distortion and the bond length in the CoO_6 octahedra.[10] Muller and Roy[11] established a structural field map to outline the stability of different ternary oxide families, among them perovskites, using ionic radii of two cations. An empirical structure map was proposed also by Li *et al.*[12] and recently by Zhang *et al.*[13] for >300 perovskites using the bond-valence model. Despite these structural field maps becoming increasingly elaborate, it is difficult to predict the occurrence and stability of perovskite structures and even more difficult to predict their functional properties.

The $ACoO_{3-\delta}$ perovskites show a unique behavior of electrical conductivity and therefore electronic structure.[14–17] All cobalt-containing perovskites are intrinsic semiconductors at room temperature.[18–22] The spin state of Co in $LaCoO_{3-\delta}$ has been discussed widely in the literature.[14,18,23–44] At temperatures up to around −180 °C, Co is in the low-spin state ($t_{2g}{}^6e_g{}^0$, $S = 0$). At higher temperatures the spin state changes, but so far no agreement on its exact state has been reached. This spin state transition at low temperature causes an increase in the energy gap, as well as in the electrical conductivity, as shown later in this paper. For $ACoO_{3-\delta}$ perovskites, the spin state transition temperature depends on the size of the rare earth cation. With a further increase in temperature to between 270 °C and 450 °C,

the perovskites undergo a transition from a semiconductor to a metal-like conductor. Kamata *et al.*[45] correlated for simple ABO_3 compounds the state of the electrons and thereby the character of the electrical conductivity—"localized" or "itinerant" electrons—with the field strengths of the *A*- and *B*-site cations, which is the ratio of their charge or radius. With increasing radii of *A*, the Co–O bond length and Co-O-Co bond angle increase. Therefore, orbital overlap decreases at room temperature; correspondingly, the semiconductor–metal transition occurs at lower temperature.

In this paper, the influence of the size and 4*f* occupancy of the lanthanide *A* cation in the $ACoO_{3-\delta}$ perovskites on their oxygen nonstoichiometry, thermodynamic stability, electrical conductivity, and electronic structure is examined, as are the orbital interactions. As such, the *A* cation was varied from lanthanum over praseodymium, neodymium, and samarium to gadolinium with cobalt as the *B* cation. All of these compositions lie on a line in Kamata *et al.*'s structural field map.[45] $LaCoO_{3-\delta}$ is positioned closer to the line dividing the perovskites with localized and itinerant electrons than $GdCoO_{3-\delta}$. We propose that the separation line shifts with increasing temperature to higher field strengths—i.e., to the upper right area in this structural field map for the complex perovskite compositions.

II. EXPERIMENTAL METHODS

A. Preparation

For powder preparation, the combined citric acid and ethylenediaminetetraacetic acid (EDTA) complexing method was used.[46,47] For the preparation of $ACoO_{3-\delta}$, EDTA (Acros Organics, ACS reagent) was dissolved in a 25% aqueous ammonia solution (Merck, p.a.). The lanthanide nitrates—$La(NO_3)_3$, $Pr(NO_3)_3$, $Nd(NO_3)_3$, and $Sm(NO_3)_3$ (Sigma-Aldrich, 99.9%) and $Gd(NO_3)_3$ (ABCR, 99.9%)—and cobalt nitrate or $Co(NO_3)_2$ (Fluka, $\geqslant$98%) were dissolved in water after determining the exact water content of the starting materials with differential thermal analysis/thermogravimetry (DTA/TG) (Netzsch STA 449C). After obtaining a clear solution, the nitrate solution and citric acid monohydrate (Fluka, $\geqslant$99.5%) were added to the EDTA solution while stirring. The desired molar ratio of metal ions to EDTA to citric acid was 1:1:1.5. The purple solution was heated in an oil bath to 80 °C. After 5 h, the temperature was increased to 140 °C and held overnight. The resulting dark brown foam was then calcined in a furnace (Nabertherm L3). For calcination, the furnace was heated at 3 °C/min to 1100 °C for 2 h in ambient air. Around 600 °C, the release of gases during the decomposition of the precursor led to an expansion of the foam. After calcination, the resulting powder was dry milled in an agate mortar. For electrical conductivity measurements, the powders were pressed in bars with the dimension 55 × 5 × 3 mm in an axial press at a pressure of 45 kN. For one bar, 3.0 g of perovskite powder was used. The bars were sintered at 1100 °C for 48 h at a 3 °C/min heating and cooling rate.

B. Characterization

The phase purity was determined by x-ray diffraction (XRD, STOE STADI P2) with Cu K_α radiation. For data processing and generating XRD patterns, WinX^{POW} from Stoe was used. XRD patterns were analyzed with COMPARIS[48] and matched to known patterns from the International Centre for Diffraction Data. The microstructure was determined by field emission gun scanning electron microscopy (LEO Gemini 1530) with secondary electron detection.

The porosities of the sintered bars were measured using Archimedes' principle. The linear shrinkage was determined by measuring the geometry of the bar before and after sintering. Electrical conductivity was measured in four-point direct current mode in air with a multimeter 2001 from Keithley. The conductivity was measured as a function of temperature $\leqslant$ 1000 °C at heating and cooling ramp of 3 °C/min. For the soft x-ray absorption spectroscopy (XAS) measurements, the bars were used as sintered; these samples are noted as "25 °C" in the XAS measurements. One half of each bar was heated to 800 °C for 300 h in air and was air quenched to room temperature. These samples are noted as "800 °C" for the XAS. XRD patterns were taken of $LaCoO_{3-\delta}$, $PrCoO_{3-\delta}$, and $GdCoO_{3-\delta}$ air quenched from 800 °C to determine whether any phase change occurred as a result of the temperature treatment. The XAS measurements were made at the Daresbury Laboratory Synchrotron Radiation Source on beamline 1.1, equipped with a high-energy spherical grating monochromator. The ring energy was 2.0 GeV, producing a current range of ~150–200 mA. The oxygen *K* edge at 530 eV and cobalt $L_{II,III}$ edge at 780 eV were examined for $ACoO_{3-\delta}$ with A = La, Pr, Nd, Sm, and Gd. The $M_{IV,V}$ edges were also recorded at energies of ~830–1070 eV for La, Pr, Nd, Sm, and Gd. The energy resolution of the beamline with a 0.1 mm exit slit was ~0.25 eV and 0.45 eV at a x-ray energy of 530 eV and 780 eV, respectively. The XAS was measured in total electron yield mode in a vacuum better than 10^{-5} Pa, with five samples held in the vacuum chamber at once. The samples were measured at room temperature. Just before measuring, the samples were crushed into a loose powder, spread thinly on a piece of carbon tape, mounted to the sample holder, and put into the vacuum chamber. For analysis, the spectra were background subtracted and normalized to the intensity 40–80 eV above the edge. The first peak in the O *K* spectra was fitted with two Gaussian curves after the edge step was fitted with an arctangent function, and the contribution from the carbon tape or residual CO_2 was fitted with one Gaussian.

The weight change during reduction of the samples was measured with simultaneous DTA/TG using a Netzsch STA 449 C Jupiter equipped with a rhodium–platinum furnace in a dynamic atmosphere. The gas flow during reduction reaction measurements was a mixture of helium with a flow of 30 sccm and 10 vol.% hydrogen in helium with a flow of 30 sccm. For measurements and corrections, identical conditions were set. For data processing and analyses, the Proteus Analysis program from Netzsch was used. Before these measurements, the perovskite powders were dried in an inert He atmosphere at 300 °C. The measurements were done in reducing atmosphere at a heating rate of 5 °C/min to 850 °C, followed by 30 min of dwell at the highest temperature.

The solid-oxide electrolyte galvanic cells method was employed to obtain the thermodynamic properties of the samples. As shown in previous papers,[49–52] the thermodynamic stability limits of the $ABO_{3-\delta}$ perovskite-type oxides are conveniently situated within the range of oxygen chemical potentials that

can be measured using galvanic cells containing 12.84 wt.% yttria-stabilized zirconia solid electrolyte and an iron–wüstite reference electrode. The design of the apparatus, as well as the theoretical and experimental considerations related to the applied method, was previously described.[49,50] Measurements were performed in vacuum at a residual gas pressure of 10^{-5} Pa. The electromotive force (EMF) was measured with a Keithley 2000 multimeter at 50 °C intervals between 600 °C and 1000 °C, each time waiting until equilibrium conditions were obtained. Equilibrium conditions were achieved when values for increasing and decreasing temperatures agreed within 1 or 2 mV in the EMF. Three independent series of measurements were carried out for each composition. By using the experimental values of the EMF of the cell and knowing the partial pressures associated with the iron–wüstite equilibrium,[53–55] the oxygen dissociation pressures of $ACoO_{3-\delta}$ ternary oxides, as well as the Gibbs free energy of decomposition, were determined according to known relationships.[51]

III. RESULTS AND DISCUSSION

A. Microstructure

Figure 1 shows the XRD patterns of the calcined $ACoO_{3-\delta}$ powders, which were all single phase. In the series from La to Gd, we observe a symmetry change from rhombohedral to orthorhombic because of the decreasing cation size on the *A* site, in accordance with the literature.[20,21,25,56–58] The pattern for $LaCoO_{3-\delta}$ shows peak splitting because of the lower symmetry of the rhombohedral structure versus the cubic. $SmCoO_{3-\delta}$ and $GdCoO_{3-\delta}$ show an orthorhombic crystal structure in good agreement with the literature data.[20,56,58]

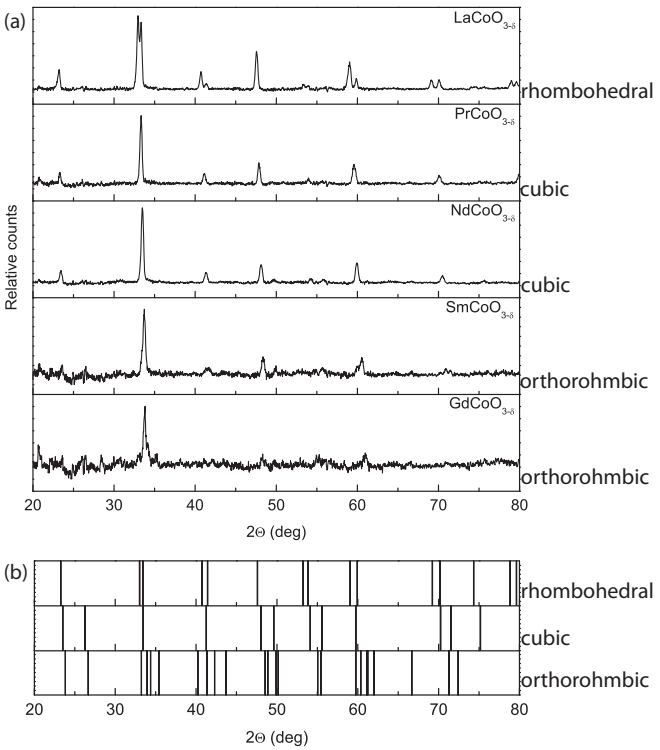

FIG. 1. (a) XRD powder pattern of the calcined (1100 °C in air) single-phase perovskites $ACoO_{3-\delta}$ (A = La, Pr, Nd, Sm and Gd). (b) Bragg positions of the different phase symmetries.

TABLE I. Porosity of the $ACoO_{3-\delta}$ perovskites calculated from the theoretical crystallographic (Ref. 59) and Archimedes density after sintering for 2 h at 1100° C (at 3 °C/min heating and cooling rate). Linear shrinkage over the width of the bars during sintering is also shown.

$ACoO_{3-\delta}$	Porosity (wt.%)	Linear shrinkage (%)
$LaCoO_{3-\delta}$	27	1.6
$PrCoO_{3-\delta}$	18	8.4
$NdCoO_{3-\delta}$	24	5.4
$SmCoO_{3-\delta}$	22	8.6
$GdCoO_{3-\delta}$	27	7.8

$PrCoO_{3-\delta}$ and $NdCoO_{3-\delta}$ show cubic symmetry with broad peaks, which indicate a change to the orthorhombic symmetry. In the literature, orthorhombic and cubic crystal symmetries are reported for these perovskites.[21,25,56–58]

B. Electrical conductivity

For the calculation of the electrical conductivity of the perovskites $ACoO_{3-\delta}$, the porosity had to be considered. The porosity of the sintered perovskite bars calculated from the theoretical crystallographic[59] and the Archimedes density was between 18 and 27 vol.%, and the linear shrinkage of the width of the bars during sintering was between 1.6% and 8.6%. The values for each composition are shown in Table I. The low degree of compaction and the occurrence of porosity were confirmed in all cases via scanning electron micrographs (SEM). A typical micrograph is shown in Fig. 2 for $LaCoO_{3-\delta}$.

In a two-phase material, consisting of an electrically conductive (perovskite) and a nonconductive phase (porosity), the effective conductivity is given by[60]

$$\sigma_{\text{eff}} = \frac{3}{2}\sigma_{\text{Perovskite}}\left(1 - por - \frac{1}{dim}\right), \tag{2}$$

where σ_{eff} is the measured conductivity of the two-phase material, $\sigma_{\text{Perovskite}}$ is the electrical conductivity of the perovskite, *por* is the fraction of porosity, and for a three-dimensional sample, *dim* is equal to 3.

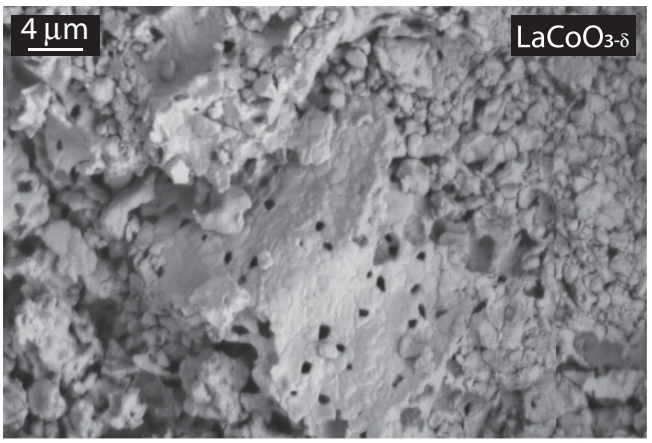

FIG. 2. SEM of an unpolished fracture surface of a sintered $LaCoO_{3-\delta}$ perovskite bar.

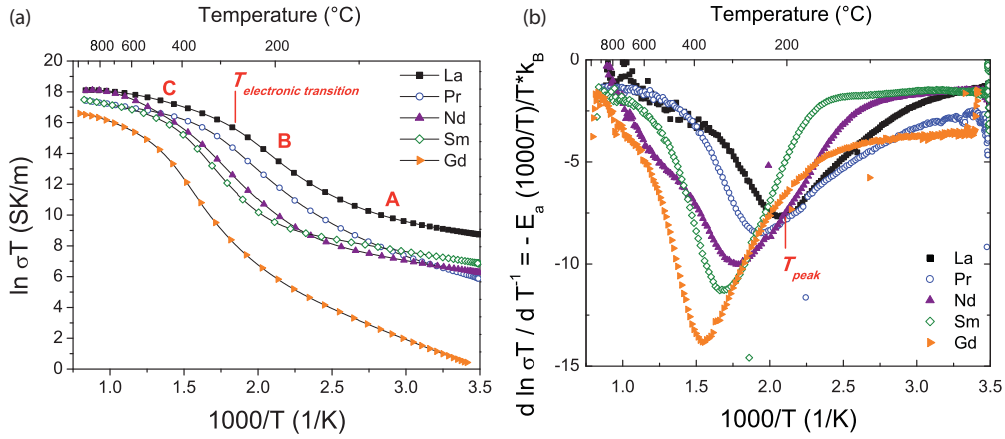

FIG. 3. (Color online) (a) Electrical conductivity and (b) derivative of ln σ T with respect to T^{-1} of $ACoO_{3-\delta}$ (A = La, Pr, Nd, Sm, and Gd) measured in air. The regions A, B, and C; transition temperature $T_{\text{electrical transition}}$; and peak temperature T_{peak}, at which the activation energy was calculated, are denoted for $LaCoO_{3-\delta}$.

The Arrhenius plot of the conductivity—as ln σT (SK/m) versus $1000/T$ (1/K)—for the $ACoO_{3-\delta}$ perovskites is plotted with respect to the A cation in Fig. 3(a). All samples showed an electrical conductivity that increases with increasing temperature. Two intrinsic regions around 100 °C–200 °C (A) and 150 °C–450 °C (B) in the plot can be distinguished, as shown in Fig. 3(a) for $LaCoO_{3-\delta}$. All investigated perovskites exhibit semiconductor properties at temperatures <500 °C with two different activation energies. According to the literature,[18–22] these two regimes can be attributed to changes in the spin state (Sec. III C). At higher temperatures, denoted as region C (>400 °C), the perovskites behave like a metallic conductor, showing nonlinearity and a slope that becomes less temperature dependent. This behavior and the absolute values of the electrical conductivities are in good agreement with previous results.[18–22]

The transition temperatures $T_{\text{electrical transition}}$ and the activation energies E_a are listed in Table II. To analyze the transition from semiconduction to metallic conduction in a more detailed way, the derivative of the conductivity was plotted as a function of $1/T$ and is shown in Fig. 3(b). With decreasing radius of cation A (from La to Gd), larger activation energies were found for the semiconductivity and the transition to metallic-like conductance occurs at higher temperatures. The peak minima, denoted as T_{peak} and where $\frac{d \ln \sigma T}{dT^{-1}}$ = constant, were used to calculate the activation energies with the Arrhenius correlation in the intermediate temperature range. The transition temperature from metallic to semiconducting behavior was ascertained in a similar way, with the slope of Fig. 3(b) plotted against $1/T$ (not shown here). The peak minima appear where the transition from metallic to semiconducting behavior takes place, listed in Table II as $T_{\text{electrical transition}}$ and where $\frac{d^2 \ln \sigma T}{d(T^{-1})^2}$ = constant. Table II also shows that with increasing ionic radius of the A cation (from Gd to La) and increasing pseudocubic lattice constant calculated from the cell volume, the activation energy and the transition temperature decrease. This implies that the activation energy and the transition temperature increase with lower symmetry.

The metallic conductivity mechanism of these perovskites results from the formation of interatomic bands caused by the overlap of the Co $3d$ t_{2g} and O $2p$ orbitals.[61,62] In the case of $ACoO_{3-\delta}$ materials, this means that decreasing the A ionic radius (increasing the A atomic number) leads to a smaller B–O–B bond angle, which is also reflected in a

TABLE II. Comparison of the different properties of the perovskite $ACoO_{3-\delta}$ (A = La, Pr, Nd, Sm and Gd), where the radius of the A cation is r_A, the bond angle Co-O-Co is α, the pseudocubic lattice constant is plc, the Goldschmidt tolerance factor is t, the Gibbs free energy change of decomposition at 850 °C is $\Delta_d G^0$ at 850 °C, the spin transition temperature is $T_{\text{spin transition}}$, the peak temperature is T_{peak}, the activation energy is E_a, the transition temperature is $T_{\text{electrical transition}}$, and the oxygen nonstoichiometry is δ.

$ACoO_{3-\delta}$	r_A[76] (Å)	α (deg)	plc[a] (Å)	t[b]	$\Delta_d G^0$ at 850 °C (kJ/mol)	$T_{\text{spin transition}}$ (°C)	T_{peak}[c] (°C)	E_a[c] (this study) (eV)	E_a (Ref.) (eV)	$T_{\text{electrical transition}}$[d] (°C)	δ
$LaCoO_{3-\delta}$	1.36	164[14]	3.83	0.971	42.37	-173[57]	212	0.66	0.46[18], 0.56[19]	269	0.008
$PrCoO_{3-\delta}$	1.32	158[63]	3.79	0.958	35.71	-73[57]	243	0.73	-	314	0.010
$NdCoO_{3-\delta}$	1.27	-	3.77	0.939	35.07	27[57,75]	293	0.86	0.74[19]	360	0.015
$SmCoO_{3-\delta}$	1.24	-	3.76	0.929	27.76	-	322	0.97	0.89[22], 0.89[20]	406	0.018
$GdCoO_{3-\delta}$	1.22	150[16]	3.74	0.920	26.54	277	374	1.20	0.93[19], 1.18[21]	452	0.032

[a]Pseudo-cubic lattice constant, plc, was calculated from the cell volume.
[b]Goldschmidt tolerance factors, t, for lanthanide-cobalt-based perovskites calculated using the effective ionic radii based on Ref. 76.
[c]Where $\frac{d \ln \sigma T}{dT^{-1}}$ = constant.
[d]Where $\frac{d^2 \ln \sigma T}{d(T^{-1})^2}$ = constant.

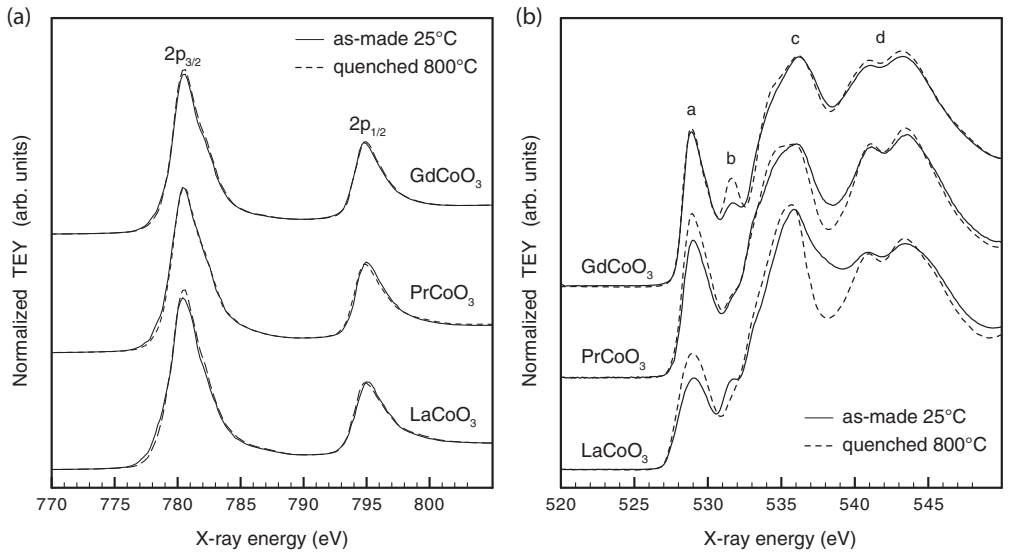

FIG. 4. (a) Co $L_{\mathrm{II,III}}$ XAS of $LaCoO_{3-\delta}$, $PrCoO_{3-\delta}$, and $GdCoO_{3-\delta}$ at 25 °C (as-made, solid line) and quenched from 800 °C (dashed line), showing the splitting of the peaks into the $2p_{1/2}$ and $2p_{3/2}$ components. The shape is like that of other samples with Co^{3+}. (b) O K XAS of $LaCoO_{3-\delta}$, $PrCoO_{3-\delta}$, and $GdCoO_{3-\delta}$ at 25 °C (as-made, solid line) and quenched from 800 °C (dashed line).

change in structural symmetry (Table II).[36] The average B–O bond length is basically constant, with a changing A ionic radius.[63] Such a trend was also observed in perovskites with the formula $ABO_{3-\delta}$ and Ti and Fe as B cations.[64,65] The deviation of the B–O–B bond angle from 180° decreases the conduction bandwidth and tends toward more insulating behavior, which corresponds to a higher transition temperature with decreasing r_A. Heating the material expands the overall structure and allows the relaxation of the bond angles toward 180°, where maximal Co $3d$ – O $2p$ – Co $3d$ overlap occurs and the conduction pathways are maximal. Decreasing the A ionic radius corresponds to increasing semiconductor–metal transition temperatures and activation energies, as was also shown in the $ANiO_{3-\delta}$ series of perovskites.[66] Nevertheless, no crystallographic change in symmetry was observed in the XRD pattern at 800 °C compared to 25 °C, which is in contrast to $YNiO_{3-\delta}$.

C. Electronic structure

Figure 4(a) shows a Co $L_{\mathrm{II,III}}$ XAS spectrum representative for the $ACoO_{3-\delta}$ samples, which yields two peaks arising from transitions from $2p^6 3d^n$ to $2p^5 3d^{n+1}$ split by the spin-orbit coupling of the core hole. As such, the shape and relative intensity of the two peaks give information about the oxidation and spin states of the probed element. The change in the oxidation state, e.g., from Co^{3+} to Co^{2+}, would lead to a shift of ∼5 eV.[67] Here, the spectra show that the Co ions remain in an average or formal 3+ state in both the semiconducting and the metallic regimes of temperature (25 °C vs 800 °C), as expected and in agreement with previous studies.[28] The samples denoted as "as-made 25 °C" were sintered for 48 h at 1100 °C and slowly cooled at a rate of 3 °C/min. The samples denoted "quenched 800 °C" were quenched in air from 800 °C to freeze the high-temperature state. It has been debated whether $ACoO_{3-\delta}$ materials exhibit charge disproportionation with increasing temperature,[18,43,68] but Abbate *et al*. similarly did not see evidence for this in the Co $L_{\mathrm{II,III}}$ XAS.[28] The energy resolution of 0.45 eV in the present spectra is not high enough to probe the spin state and partial change in the oxidation state of the Co ions via the $L_{\mathrm{II,III}}$ x-ray absorption. The shape of the white lines did not change with the rare earth ion or the quenching from 800 °C employed here. The lanthanide $M_{\mathrm{IV,V}}$ white lines (spectra not shown) also did not change as a result of the quenching. Regarding the variation of the A site in $ABO_{3-\delta}$, the smaller the ion and larger the atomic number, the more the room-temperature ground state is dominated by the low-spin Co^{3+} configuration; for A = Nd the low spin predominates, and when A = La the intermediate spin is in the majority.[25,57] The higher-Z lanthanides, from Tb onward, show the low-spin Co^{3+} at room temperature,[63] so it is likely that $GdCoO_{3-\delta}$ also is entirely low spin. Fig. 4(b) shows the O K XAS from $LaCoO_{3-\delta}$, $PrCoO_{3-\delta}$, and $GdCoO_{3-\delta}$ both at 25 °C and as quenched from 800 °C. Spectra from $NdCoO_{3-\delta}$ and $SmCoO_{3-\delta}$ were recorded but are not shown here, because they were overlapped by harmonics of the lanthanide $M_{\mathrm{IV,V}}$ peaks. The major features are labeled from lowest to highest energy as a, b, c, and d. The general shape is in agreement with previous studies.[28,37,69,70] Peak a (∼528.5 eV) is a result of the hybridization of the Co $3d$ with the O $2p$ orbitals, while peaks c and d show the contribution of the rare earth $5d$ and Co $4sp$ orbitals, respectively. Peak b is not typically seen in the O K spectra of similar perovskite samples and is here attributed to surface contamination from the carbon tape adhesive or species adsorbed on the samples, such as CO_2.

The Co $3d$ component increases in overall intensity and becomes less symmetrical by varying the rare earth ion from La over Pr to Gd. This correlates with the Goldschmidt tolerance factor and the pseudocubic lattice constant (Table II). For the rare earth $5d$ peak, its intensity relative to the Co $4sp$ peaks decreases as La > Gd > Pr, and the higher-energy peak of the Co $4sp$ pair moves to slightly lower energies as La > Pr >

Gd. In addition, a shoulder on the low-energy side of the rare earth 5*d* peak grows in intensity relative to the main peak for $PrCoO_{3-\delta}$ and $GdCoO_{3-\delta}$. These changes occur similarly in both the 25 °C and the 800 °C samples.

Looking at the $LaCoO_{3-\delta}$ O *K* XAS, the sample quenched from 800 °C has a larger contribution from the Co 3*d* orbitals than in the nonquenched, 25 °C sample. This is also true, but to a lesser extent, for $PrCoO_{3-\delta}$, but this is not observed for $GdCoO_{3-\delta}$. The rare earth 5*d* peaks do not change much with regard to temperature, but the Co 4*sp* peaks appear sharper at 800 °C than at 25 °C, with the effect greatest for $LaCoO_{3-\delta}$ and least for $GdCoO_{3-\delta}$, in contradiction to soft XAS of $LaCoO_{3-\delta}$ with *in situ* heating.[28] XRD of some quenched samples (A = La, Pr, and Gd) showed that no phase changes were associated with the high-temperature treatment.

In examining the O *K* XAS, we can gain some insight into the interaction of the Co 3*d*–O 2*p* hybridization and hole states, because the spectra reflect the interaction of the unoccupied O 2*p* states with the Co and *A* bands. Looking at the contribution of the Co 3*d* levels to the O *K* spectra (peak a), it is clear that the total 3*d* bandwidth is largest for $LaCoO_{3-\delta}$. Abbate *et al.*[28] showed that from −193 °C to 25 °C the 3*d* peak solely results from the unoccupied e_g sub-band, but temperatures of 277 °C–357 °C resulted in the development of holes in the t_{2g} sub-band, indicating a higher spin state. In the ongoing debate about the spin transitions in $LaCoO_{3-\delta}$, others have suggested that at room temperature an intermediate spin is present.[31–34] In another XAS study, Saitoh *et al.* were not able to resolve the splitting of the e_g–t_{2g} levels in the O *K* spectra of $LaCoO_{3-\delta}$ at 25 °C.[39] The spectrum of $LaCoO_{3-\delta}$ at 25 °C shown in the present study is much like that of Saitoh *et al.* and could be interpreted as resulting from either a primarily low-spin Co^{3+}, fitted with one Gaussian, or a mixed/intermediate spin with poorly resolved features. Comparing the different perovskites, a sharpening of the peak a from La to Gd is present, which indicates a smaller bandwidth because of a higher localization and therefore less hybridization. The peak area does not change significantly, because the oxidation state, and therefore the number of unoccupied states, stays the same.

If in the data presented here the first peak of the $LaCoO_{3-\delta}$ O *K* spectrum at 25 °C is taken to represent only the unoccupied e_g states, it can be fitted with a single Gaussian curve. Then the difference in intensity, energy, and width between the 25 °C spectrum and the 800 °C spectrum represents the addition of holes or change in the bandwidth that accompanies the semiconductor-to-metal transition. The same idea can be applied to the spectra of $PrCoO_{3-\delta}$ and $GdCoO_{3-\delta}$, where at 25 °C the former has more low-spin Co^{3+} character than $LaCoO_{3-\delta}$ and the latter is entirely low spin. In comparing the 25 °C spectra to the 800 °C quenched spectra, the amount of unoccupied states added by the quenching process is largest for $LaCoO_{3-\delta}$ and nearly zero for $GdCoO_{3-\delta}$. This agrees with the conductivity data, which show the lowest temperature for the semiconductor to *p*-type metal transition for $LaCoO_{3-\delta}$ and highest for $GdCoO_{3-\delta}$. It is possible that the number of holes added to each material via high-temperature quenching is the same but is not reflected in the O *K* spectra because of the decreasing *B*–O–*B* bond angle. As discussed earlier, the more this angle deviates from 180°, the less overlap and hybridization occur between Co and O. However, if the number of holes added was ion independent, the "extra" not observed in the O XAS would be primarily of a Co 3*d* character, and this should induce some change in the Co $L_{II,III}$ spectra, which was not observed. So, for the samples quenched from 800 °C, the holes created belong to hybridized O 2*p*–Co 3*d* (t_{2g}) states, with the number of holes created decreasing with an increasing lanthanide atomic number, resulting in lower total conductivity and higher transition temperatures.

D. Thermodynamic stability

The mass loss in a reducing atmosphere was measured as a function of time to ascertain the oxygen nonstoichiometry δ of the perovskites $ACoO_{3-\delta}$. The thermogravimetry (TG) mass loss curves of $ACoO_{3-\delta}$ perovskites with respect to temperature are displayed in Fig. 5(a). The mass loss was between 8.5 and 9.5 wt.% at 800 °C. The experiments were carried out with the calcined powders in a reducing atmosphere made up by 5 vol.% H_2 in He. The oxygen partial pressure calculated from the gas ratio was lower than 10^{-18} bar at all temperatures. Up to 350 °C, all perovskites remained stable and no mass loss could be detected. All perovskites started to decompose at roughly the same rather low temperature of ∼350 °C in this reducing atmosphere. Presumably, decomposition does not take place <350 °C for kinetic reasons. At higher

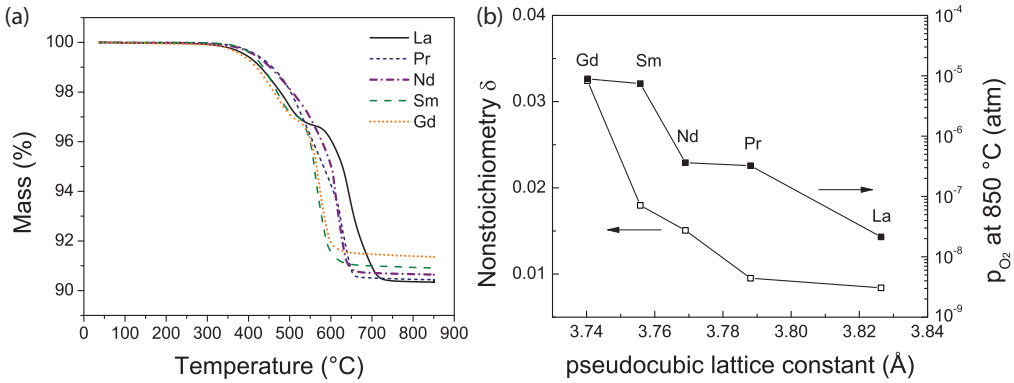

FIG. 5. (Color online) (a) $ACoO_{3-\delta}$ (A = La, Pr, Nd, Sm, and Gd) mass loss over temperature as measured by TG in helium with 5 vol.% hydrogen. (b) Nonstoichiometry δ and oxygen partial pressure at 850 °C of $ACoO_{3-\delta}$ (A = La, Pr, Nd, Sm, and Gd) vs pseudocubic lattice constant.

temperatures (>350 °C), pronounced mass losses occurred until a stable mass of roughly 91 wt.% is reached around 650 ± 50 °C. The mass losses occur in two steps according to the reaction:

$$ACoO_{3-\delta} \rightleftarrows \frac{1}{2}A_2O_3 + CoO + \frac{0.5-\delta}{2}O_2 \rightleftarrows \frac{1}{2}A_2O_3 + Co + \frac{1.5-\delta}{2}O_2. \quad (3)$$

In the first step, the samples decompose into the corresponding lanthanide oxide and cobalt(II) oxides; in the second step, the latter is reduced to metallic cobalt. For $PrCoO_{3-\delta}$ and $NdCoO_{3-\delta}$, the two steps are poorly resolved in the TG signal. From previous reports on $LaCoO_{3-\delta}$, it is known that a stable mass is reached once decomposition into the lanthanum oxide and metallic cobalt is achieved, which was proved by XRD.[71–74] The calculation of oxygen nonstoichiometry of the original perovskites is based on the total decomposition reaction (Eq. (3)) and the masses measured at 200 °C and 800 °C.

In order to obtain further insight into the physical mechanisms explaining the behavior of the $ACoO_{3-\delta}$ perovskites, the thermodynamic data represented by the oxygen dissociation pressure, as well as the Gibbs free energy change of decomposition, $\Delta_d G^0$, were determined from the experimental equilibrium EMF values (Table II). The oxygen dissociation pressures p_{O_2} of the samples were calculated by the Nernst equation:

$$E = \frac{RT}{4F} \ln \frac{p_{O_2}}{p_{O_2(ref)}}, \quad (4)$$

where p_{O_2} and $p_{O_2(ref)}$ are the oxygen partial pressures of the sample and the reference electrode, respectively. R is the universal gas constant, F is the Faraday constant, and T is the absolute temperature in Kelvin. The measurements refer to the temperature ranges of 700 °C–900 °C for A = La, Pr, and Nd; 800 °C–950 °C for A = Sm; and 800 °C–900 °C for A = Gd. In the temperature ranges investigated, the decomposition reaction of $ACoO_{3-\delta}$ is represented by the first reaction step of Eq. (3). The standard Gibbs free energy change of decomposition is obtained from Eq. (5):

$$\Delta_d G^0 = -\frac{0.5-\delta}{2} RT \ln p_{O_2}. \quad (5)$$

In the investigated temperature ranges, the logarithms of the dissociation pressure increase with increasing temperature for all systems. The experimental values of the oxygen dissociation pressure at 850 °C and the calculated oxygen nonstoichiometry δ as a function of the pseudocubic lattice constant are plotted in Fig. 5(b). The nonstoichiometry δ and log p_{O_2} are higher, and the thermodynamic stability is therefore lower, for the compounds with smaller radii of the A cation. We conclude that the thermodynamic stability as well as the oxygen nonstoichiometry and the electrical properties, depend on the crystal structure, which is specified through the pseudocubic lattice constant and the Co–O–Co bond angle (Table II).

IV. CONCLUSIONS

Structural, electrical, and thermodynamic properties are summarized in Table II. We conclude that the electrical behavior and the thermodynamic properties of perovskites with the formula $ACoO_{3-\delta}$ (A = La, Pr, Nd, Sm, and Gd) are linked to the amount of distortion of the crystal lattice in the materials. Because of a higher distortion from La to Gd, the Co–O–Co bond angle and the pseudocubic lattice constant decrease and lower the overlap of the cobalt 3d and oxygen 2p orbitals. Therefore, a lower hybridization of the 3d orbitals of the cobalt cation with the 2p orbitals of the oxygen anion is present. A lower overlap causes lower electrical conductivity and higher activation energy of the semiconductivity. As the radius of the A cation decreases from La to Gd, the volume of the unit cell also decreases. In parallel to the unit cell volume change, the distortion in the orthorhombic structures increases through the tilting of the BO_6 octahedra. Both facts lead to a higher oxygen nonstoichiometry and a lower standard Gibbs free energy of the decomposition of perovskites from $LaCoO_{3-\delta}$ to $GdCoO_{3-\delta}$.

In order to be a good cathode material for SOFCs, high electrical conductivity and high catalytic activity are favorable. $LaCoO_{3-\delta}$ has the highest electrical conductivity; therefore, it should be the best cathode material among those studied in this paper. However, the oxygen nonstoichiometry is highest for $GdCoO_{3-\delta}$, which could lead to better oxygen-ion conductivity and catalytic activity.

ACKNOWLEDGMENTS

The authors thank Anna Evans, Toni Ivas, and and Jennifer Rupp from the Nonmetallic Inorganic Materials Group of ETH Zurich (Switzerland) for stimulating discussions and M. Wörle and R. Nesper from the Inorganic Solid State Chemistry laboratory of ETH Zurich (Switzerland) for the use of the x-ray diffractometer. The synchrotron work was performed on beamline 1.1 of the Daresbury Laboratory Synchrotron Radiation Source (SRS), and the authors thank beamline scientist John A. Purton. The authors acknowledge financial support by the Swiss National Science Foundation for the program: Scientific Co-operation between Eastern Europe and Switzerland (SCOPES 2009-2012): Joint Research Project (JRP) Project No. IZ73Z0_128185/1, the UK Science and Technology Facilities Council under SRS Project No. 47093, the Commission for Technology and Innovation, and the Center of Competence Energy and Mobility.

*Barbara.Scherrer@mat.ethz.ch

[1] L. J. Gauckler, D. Beckel, B. E. Buergler, E. Jud, U. P. Muecke, M. Prestat, J. L. M. Rupp, and J. Richter, CHIMIA Int. J. Chem. **58**, 837 (2004).

[2] T. Arakawa, H. Kurachi, and J. Shiokawa, Appl. Phys. Lett. **47**, 1183 (1985).

[3] M. S. Spencer and M. V. Twigg, Annu. Rev. Mater. Res. **35**, 427 (2005).

[4] C. N. R. Rao, A. K. Cheetham, and R. Mahesh, Chem. Mater. **8**, 2421 (1996).

[5] Z. Fisk and J. L. Sarrao, Annu. Rev. Mater. Sci. **27**, 35 (1997).

[6] M. Sambridge, Science **299**, 529 (2003).

[7] A. R. Oganov and S. Ono, Nature **430**, 445 (2004).

[8] M. Murakami, K. Hirose, K. Kawamura, N. Sata, and Y. Ohishi, Science **304**, 855 (2004).

[9] V. Goldschmidt, Skr. Norske Vidensk.-Akad. I. Mat. Naturv. Kl. **8**, (1926).

[10] M. Yoshimura, T. Nakamura, and T. Sata, Bull. Tokyo Inst. Tech. **120**, 13 (1974).

[11] O. Muller and R. Roy, *The Major Ternary Structural Families* (Springer-Verlag, Berlin, 1874).

[12] C. Li, K. C. K. Soh, and P. Wu, J. Alloys Compd. **372**, 40 (2004).

[13] H. Zhang, N. Li, K. Li, and D. F. Xue, Acta Crystallogr. B **63**, 812 (2007).

[14] G. Thornton, B. C. Tofield, and A. W. Hewat, J. Solid State Chem. **61**, 301 (1986).

[15] S. Yamaguchi, Y. Okimoto, H. Taniguchi, and Y. Tokura, Phys. Rev. B **53**, R2926 (1996).

[16] S. Yamaguchi, Y. Okimoto, and Y. Tokura, Phys. Rev. B **54**, 11022(R) (1996).

[17] J. Zaanen, G. A. Sawatzky, and J. W. Allen, Phys. Rev. Lett. **55**, 418 (1985).

[18] V. G. Bhide, G. R. Rao, C. N. R. Rao, and D. S. Rajoria, Phys. Rev. B **6**, 1021 (1972).

[19] D. S. Rajoria, V. G. Bhide, G. R. Rao, and C. N. R. Rao, J. Chem. Soc. Faraday Trans. 2 **70**, 512 (1974).

[20] J. W. Kang, K. H. Ryu, and C. H. Yo, Bull. Kor. Chem. Soc. **16**, 600 (1995).

[21] S. V. Kurgan, G. S. Petrov, L. A. Bashkirov, and A. I. Klyndyuk, Inorg. Mater. **40**, 1224 (2004).

[22] H. Y. Tu, Y. Takeda, N. Imanishi, and O. Yamamoto, Solid State Ionics **100**, 283 (1997).

[23] T. Kyômen, Y. Asaka, and M. Itoh, Phys. Rev. B **71**, 024418 (2005).

[24] R. J. Radwanski and Z. Ropka, Phys. B: Condens. Matter **359–361**, 1354 (2005).

[25] J. Q. Yan, J. S. Zhou, and J. B. Goodenough, Phys. Rev. B **69**, 134409 (2004).

[26] M. Zhuang, W. Zhang, and N. B. Ming, Phys. Rev. B **57**, 10705 (1998).

[27] M. A. Senaris-Rodriguez and J. B. Goodenough, J. Solid State Chem. **116**, 224 (1995).

[28] M. Abbate, J. C. Fuggle, A. Fujimori, L. H. Tjeng, C. T. Chen, R. Potze, G. A. Sawatzky, H. Eisaki, and S. Uchida, Phys. Rev. B **47**, 16124 (1993).

[29] T. Kyomen, Y. Asaka, and M. Itoh, Phys. Rev. B **67**, 144424 (2003).

[30] T. Kyomen, R. Yamazaki, and M. Itoh, Phys. Rev. B **68**, 104416 (2003).

[31] M. A. Korotin, S. Y. Ezhov, I. V. Solovyev, V. I. Anisimov, D. I. Khomskii, and G. A. Sawatzky, Phys. Rev. B **54**, 5309 (1996).

[32] M. Itoh, J. Hashimoto, S. Yamaguchi, and Y. Tokura, Phys. B: Condens. Matter **281–282**, 510 (2000).

[33] M. Motin Seikh, L. Sudheendra, C. Narayana, and C. N. R. Rao, J Mol. Struct. **706**, 121 (2004).

[34] L. Sudheendra, M. Motin Seikh, A. R. Raju, and C. Narayana, Chem. Phys. Lett. **340**, 275 (2001).

[35] S. Stolen, F. Gronvold, H. Brinks, T. Atake, and H. Mori, J. Chem. Therm. **30**, 365 (1998).

[36] D. P. Kozlenko, N. O. Golosova, Z. Jirak, L. S. Dubrovinsky, B. N. Savenko, M. G. Tucker, Y. L. Godec, and V. P. Glazkov, Phys. Rev. B: Condens. Matter **75**, 064422 (2007).

[37] O. Toulemonde, N. N'Guyen, F. Studer, and A. Traverse, J. Solid State Chem. **158**, 208 (2001).

[38] M. Itoh, M. Mori, M. Sugahara, T. Yamauchi, and Y. Ueda, Phys. B: Condens. Matter **230–232**, 756 (1997).

[39] T. Saitoh, T. Mizokawa, A. Fujimori, M. Abbate, Y. Takeda, and M. Takano, Phys. Rev. B **55**, 4257 (1997).

[40] M. Itoh and I. Natori, J. Magn. Magn. Mater. **140–144**, 2145 (1995).

[41] K. Asai, O. Yokokura, N. Nishimori, H. Chou, J. M. Tranquada, G. Shirane, S. Higuchi, Y. Okajima, and K. Kohn, Phys. Rev. B **50**, 3025 (1994).

[42] A. Podlesnyak, K. Conder, E. Pomjakushina, A. Mirmelstein, P. Allenspach, and D. I. Khomskii, J. Magn. Magn. Mater. **310**, 1552 (2007).

[43] G. Thornton, I. W. Owen, and G. P. Diakun, J. Phys. Condens. Matter **3**, 417 (1991).

[44] P. M. Raccah and J. B. Goodenough, Phys. Rev. **155**, 932 (1967).

[45] K. Kamata, T. Nakamura, and T. Sata, Bull. Tokyo Inst. Tech. **120**, 73 (1974).

[46] Z. P. Shao, W. S. Yang, Y. Cong, H. Dong, J. H. Tong, and G. X. Xiong, J. Membr. Sci. **172**, 177 (2000).

[47] H. H. Wang, S. Tablet, W. S. Yang, and R. Caro, Mater. Lett. **59**, 3750 (2005).

[48] A. Piotto Piotto, Ph.D. thesis, ETH Zurich, Nr. 15659, 2004.

[49] S. Tanasescu, N. D. Totir, and D. I. Marchidan, Mater. Res. Bull. **32**, 925 (1997).

[50] S. Tanasescu, N. D. Totir, and D. I. Marchidan, Electrochim. Acta **43**, 1675 (1998).

[51] S. Tanasescu, N. D. Totir, and D. I. Marchidan, Solid State Ionics **134**, 265 (2000).

[52] S. Tanasescu, M. N. Grecu, M. Urse, F. Teodorescu, L. M. Giurgiu, H. Chiriac, and N. D. Totir, Adv. Appl. Ceram. **108**, 273 (2009).

[53] L. S. Darken and R. W. Gurry, J. Am. Chem. Soc. **67**, 1398 (1945).

[54] C. E. Wicks and F. E. Block, U.S. Bur. Mines Bull. **605**, 57 (1963).

[55] K. K. Kelley and E. G. King, U.S. Bur. Mines Bull. **592**, 232 (1961).

[56] E. Traversa, M. Sakamoto, and Y. Sadaoka, Particul. Sci. Technol. **16**, 185 (1998).

[57] J. S. Zhou, J. Q. Yan, and J. B. Goodenough, Phys. Rev. B **71**, 220103 (2005).

[58] Y. Sadaoka, E. Traversa, and M. Sakamoto, J. Mater. Chem. **6**, 1355 (1996).

[59] F. S. Galasso, *Structure, Properties and Preparation of Perovskite Type Compounds* (Pergamon Press Lit., Headington Hill Hall, Oxford, 1969).

[60] D. Stroud, Superlattice. Microst. **23**, 567 (1998).

[61] J. Goodenough, in *Localized to Itinerant Electronic Transition in Perovskite Oxides*, edited by J. Goodenough (Springer Berlin, Heidelberg, 2001), Vol. 98, p. 1.

[62]J. Goodenough and J. S. Zhou, in *Localized to Itinerant Electronic Transition in Perovskite Oxides*, edited by J. Goodenough (Springer Berlin, Heidelberg, 2001), vol. 98, p. 17.
[63]J. A. Alonso, M. J. Martinez-Lope, C. D. L.. Calle, and V. Pomjakushin, J. Mater. Chem. **16**, 1555 (2006).
[64]D. A. Maclean, H. N. Ng, and J. E. Greedan, J. Solid State Chem. **30**, 35 (1979).
[65]M. Imada, A. Fujimori, and Y. Tokura, Rev. Mod. Phys. **70**, 1039 (1998).
[66]J. B. Torrance, P. Lacorre, A. I. Nazzal, E. J. Ansaldo, and C. Niedermayer, Phys. Rev. B **45**, 8209 (1992).
[67]D. Bazin, I. Kovács, L. Guczi, P. Parent, C. Laffon, F. De Groot, O. Ducreux, and J. Lynch, J. Catal. **189**, 456 (2000).
[68]C. Tealdi, L. Malavasi, C. A. J. Fisher, and M. S. Islam, J. Phys. Chem. B **110**, 5395 (2006).
[69]A. R. Moodenbaugh, B. Nielsen, S. Sambasivan, D. A. Fischer, T. Friessnegg, S. Aggarwal, R. Ramesh, and R. L. Pfeffer, Phys. Rev. B **61**, 5666 (2000).
[70]M. Imamura, N. Matsubayashi, and H. Shimada, J. Phys. Chem. B **104**, 7348 (2000).
[71]R. Lago, G. Bini, M. A. Pena, and J. L. G. Fierro, J. Catal. **167**, 198 (1997).
[72]T. Nakamura, G. Petzow, and L. J. Gauckler, Mater. Res. Bull. **14**, 649 (1979).
[73]M. A. Pena and J. L. G. Fierro, Chem. Rev. **101**, 1981 (2001).
[74]M. Seppanen, M. Kyto, and P. Taskinen, Scand. J. Metall. **8**, 199 (1979).
[75]X. Liu and C. T. Prewitt, J. Phys. Chem. Solids **52**, 441 (1991).
[76]R. D. Shannon, Acta Crystallogr. A **32**, 751 (1976).